



Research article

Simulation study on creep deformation of the impeller in lead-bismuth eutectic environment through fluid-solid coupling method

Cheng Gu^{a,c,*}, Weili Peng^a, Zenghui Tian^a, Jianhua Zhao^{a,b,c,**}, Fan Wang^d, Yajun Wang^a, Jiakuan Zhang^a

^a College of Materials Science and Engineering, Chongqing University, Chongqing, 400045, China

^b State Key Laboratory of Mechanical Transmission, Chongqing University, Chongqing, 400044, China

^c National Key Laboratory of Advanced Casting Technologies, Chongqing University, Chongqing, 400044, China

^d Chongqing Pump Industry Co., Ltd., Chongqing, 400033, China

ARTICLE INFO

Keywords:

Nuclear main pumps
Liquid lead-bismuth
Fluid-solid coupling
Stress deformation
Creep

ABSTRACT

Lead-based reactor is a new type of reactor using liquid lead or lead-bismuth alloy as a coolant. As the core working element of the main pump, the impeller is subjected to a huge load when conveying heavy metal liquids and is highly susceptible to damage. In this study, we used ANSYS and FLUENT software to investigate the stress, deformation, and creep deformation of the nuclear main pump impeller under a liquid lead-bismuth environment by the fluid-solid coupling method. The maximum equivalent force of the impeller was located at the junction of the blade and hub, which was prone to fatigue damage under the action of alternating load. The stress, deformation, and creep characteristics of the impeller blade were observed to generally increase with rotational speed. Particularly, the junction of the blade root and hub exhibited high susceptibility to stress concentration and fatigue damage. At a flow rate of 0.64 m/s and a speed of 690 r/min, the maximum equivalent force was 16.7 MPa, which was lower than the yield strength of 316L stainless steel. Additionally, the maximum deformation was less than 0.63 mm. Over a five-year period, the creep of the impeller ranged from a minimum of 0.228% to a maximum of 0.447%, indicating that the impeller can reliably operate in a liquid lead-bismuth environment for at least five years.

1. Introduction

The lead-based cooled fast reactor (LFR) is considered to be one of the most promising fourth-generation (Gen-IV) reactors for its potential in sustainability, economics, safety, and reliability [1–3]. In both LFR and Accelerator Driven Systems (ADS), lead alloys, particularly lead-bismuth eutectic (LBE), are considered as the primary coolant [4] since lead possesses desirable characteristics such as high density (around 10500 kg/m³), low neutron-moderating and absorption capacity, high boiling temperature (above 1700 °C), relatively low cost, and inertness with water, air, and fuel [5,6]. However, the high density and melting temperature (around 327 °C),

* Corresponding author. College of Materials Science and Engineering, Chongqing University, Chongqing, 400045, China.

** Corresponding author. College of Materials Science and Engineering, Chongqing University, Chongqing, 400045, China.

E-mail addresses: gucheng.90@cqu.edu.cn (C. Gu), zjh wzf@sina.com (J. Zhao).

<https://doi.org/10.1016/j.heliyon.2024.e26035>

Received 19 September 2023; Received in revised form 4 February 2024; Accepted 7 February 2024

Available online 8 February 2024

2405-8440/© 2024 The Authors. Published by Elsevier Ltd. This is an open access article under the CC BY-NC-ND license (<http://creativecommons.org/licenses/by-nc-nd/4.0/>).

Table 1
Material properties used in this study.

Material	Density (kg/m ³)	Poisson's ratio	Young's modulus (GPa)	Tensile strength (MPa)
316L steel	7850	0.3	193	460
	Density (kg/m ³)	Viscosity (cps)	Melting point (°C)	Boiling point (°C)
LBE	10271	0.001665	125	1670

as well as the low viscosity at operating temperatures, pose specific structural material requirements for components such as impeller blades in the reactor coolant pumps of LFR and ADS systems [1].

The main circulation pump in the reactor is very important since it supplies force for coolant circulation. As the core component of the pump, the impeller operates in a complex and harsh environment and is highly susceptible to weakening due to corrosion, erosion, fatigue, creep deformation, and more under high-temperature flowing LBE and cyclic loads [7]. It is essential to have a comprehensive understanding and accurate predictions of the stress and deformation evolution of the impeller in the LBE environment. Previous studies have successfully utilized computational fluid dynamics (CFD) simulations to analyze the behavior of various pump impellers [7,8]. Zhai et al. [9] simulated the stress distribution of the impeller considering the flow field pressure, the centrifugal force, and the gravity and established the relational expression including the fatigue life, average stress, and stress amplitude. Chen et al. [10] adopted fluid-solid coupling method to solve the fluid and solid coupling equations and found that the blade stresses in the reactor coolant pump mainly include tensile stresses caused by centrifugal forces, bending and torsional stresses caused by flow field pressure, and thermal stresses caused by the temperature field. Wang et al. [11] used fluid-solid coupling method to simulate and analyze the reactor coolant pump, and the results showed that the maximum stress and deformation of the rotor under different flow conditions were mainly distributed on the impeller and hub, with the stress concentration mainly located at the junction of the front cover and the vane outlet. Ma et al. [12] simulated the flow field of a heavy metal liquid pump and compared the stress in the liquid metal pump with that in the pump. The results showed that the maximum stress of the impeller blade increased with the increase of the flow rate. Liu et al. [13] conducted a unidirectional fluid–solid coupling analysis for the distribution of stress field and deformation of the axial-flow pump blade. The results showed that the stress concentration is found at the root of the blade near the hub, and the maximum deformation is often located on the blade surface or blade tip. Similar results on the stress and deformation characteristics of axial flow pumps under different operating conditions were obtained by other studies [14–16].

Researchers have also analyzed the stress distribution and deformation characteristics of the impeller under different working conditions of centrifugal pumps [17,18], mixed flow pumps [19], and tubular pumps [20,21] using fluid-solid coupling method. Li et al. [22] studied the effect of fluid flow on the dynamic characteristics of the pump impeller and found that radial forces were the main cause of impeller vibration. Yong et al. [23] found that the increase of the vibration mass of the whole system caused by the vibration of the water body is the root cause of the decrease of the natural frequency of the impeller. Cheng et al. [24] found that the effect of clearance ratio on the maximum equivalent force on the back surface of the impeller blade was larger than that on the working surface. Zheng et al. [25] investigated the effect of flow temperature on the reliability of centrifugal compressor impellers, showing that the effect of temperature on the strength and reliability of compressor impellers must be taken into account at high pressure ratios, and can be ignored at low pressure ratios. Meng et al. [26] studied the stress distribution and deformation of the impeller under different rotational directions, and the results showed that the maximum equivalent force increased with the increase of the flow rate. Chen et al. [27] studied the static simulation of the entire flow path of the mixed-flow pump during reverse power generation, and the results showed that the radial force acting on the blades in reverse power generation was higher, with the impeller stresses mainly concentrated at the blade edges and roots, which was also obtained by Zhou et al. [28]. Li et al. [29] investigated the modal parameters of turbocharger impellers, which showed that the fluid-solid interaction mainly affected the modal frequency. Wang et al. [30] studied the effect of impeller blade thickness on the performance of multistage centrifugal pumps through fluid-solid coupling, and the results showed that the maximum stress and deformation of the impeller progressively decreased with the increase of blade thickness, while the stability of the impeller structure increased. Although various aspects affecting the pump have been studied, there has been a lack of research that explores the creep effect on the impeller in the LBE environment. It is important to understand the creep behavior of the impeller since it keeps working for years in the nuclear reactor, while prior publications have mainly focused on simulating stress-deformation characteristics of the impeller [31–33].

In this study, we implemented a unidirectional fluid-solid coupling method to examine both the internal flow field and impeller structure field in the liquid LBE environment. We investigated the impeller's stress, strain, and creep characteristics under certain flow rates and varying speed conditions. These results provide guidance for optimizing impeller design and ensuring stable operation of the model under specific conditions.

2. Material and methods

2.1. Material

316L stainless steel was selected as the material of the impeller with the properties as shown in Table 1 [34,35]. The fluid material was chosen to be a liquid LBE alloy (Pb-55.5 wt%Bi alloy). The density of the LBE alloy can be calculated by Eq. (1) [35]:

$$\rho_{LBE} = 11096 - 1.3236T \quad (1)$$

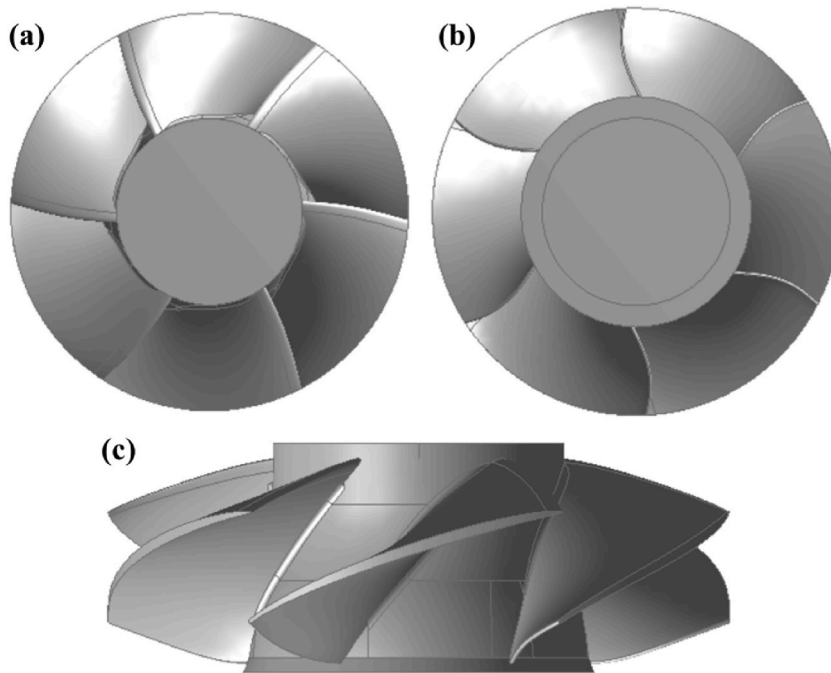


Fig. 1. Geometrical model of the impeller (a) front view, (b) back view, and (c) side view.

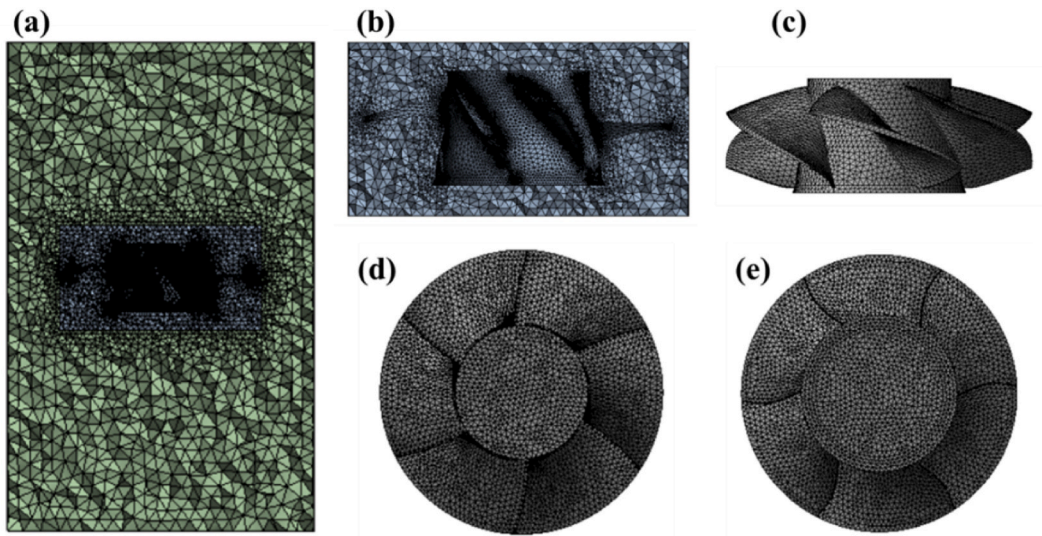


Fig. 2. Meshing of the simulation domain: (a) cross-section of the whole fluid domain, (b) cross-section of the rotor area, and meshing of the impeller in (c) side view, (d) front view, and (e) back view.

where T is the temperature (K).

2.2. Modeling and meshing

The three-dimensional model was established by the software UG as shown in Fig. 1(a–c). The parameters of the impeller model included inlet diameter of 535 mm, impeller diameter of 320 mm, hub thickness of 118 mm, and blade number of 6. It should be noted that the small features in the impeller model, such as sharp corners, mutations, gaps, were simplified accordingly.

In this study, we adopted the multiple reference coordinate system method to simulate the rotational motion of the impeller. As shown in Fig. 2(a and b), the rotating reference coordinate system is used in the region with the impeller, and the stationary reference

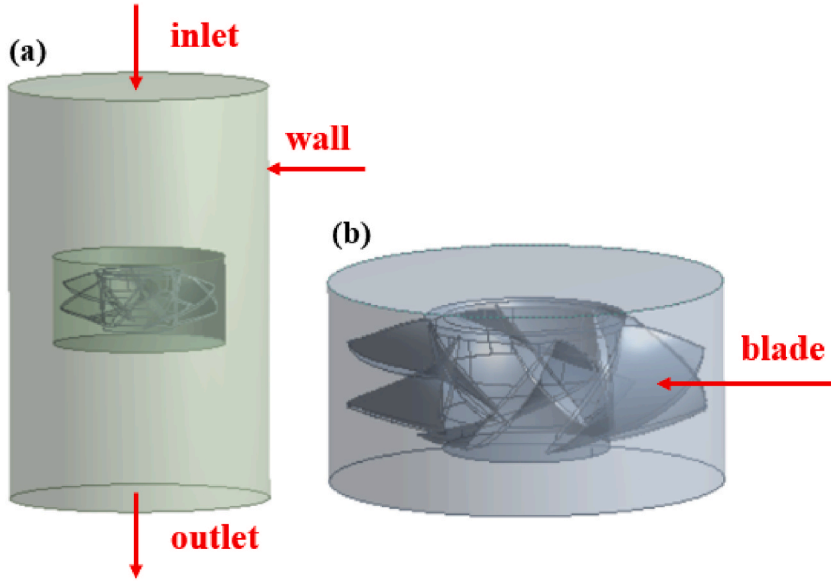


Fig. 3. Geometric model for CFD simulation domain: (a) the stator area, (b) the rotor area.

coordinate system is used in the region outside the impeller, so that the non-stationary problem in the stationary reference system can be transformed into the stationary problem in the rotating system. Therefore, the computational domain is divided into rotor and stator areas. The volume of the stator area is large, and the grid is a tetrahedral grid with a number of grid cells of 240047. The rotor area has a complex shape which is the key area of concern and requires high grid quality. The grid is a tetrahedral grid and the number of grid cells is 2092294.

The mesh quality has a great influence on the subsequent analysis results as well as the convergence of the calculation. In this study, we mainly evaluated the grid quality in terms of element quality, aspect ratio and skewness [36]. The element quality is a value between 0 and 1, with 0 being the worst and 1 being the best. The aspect ratio is the calculated length-to-width ratio (longest side/shortest side) for the triangle or quadrilateral vertices of the cell with the value no less than 1, which reaches the best quality when equal to 1. The skewness is a value between 0 and 1, with 0 being the ideal value and 1 being the worst value. When observing the size of the skewness, it is necessary to ensure that the maximum value is less than 0.94. The mean value of the element quality is 0.83 (higher than the general mean value of 0.75). The maximum value of the aspect ratio is less than 15.2. The maximum value of skewness is less than 0.85. Therefore, the quality of the grid meets the requirements, and the meshing is shown in Fig. 2(c–e). The impeller is divided by tetrahedral mesh with the mesh number of 125542.

2.3. Fluid-solid coupling

The fluid-solid coupling calculation involved parameter settings for both the fluid field and the structural field, where the fluid field calculation was performed in FLUENT module and the structural field calculation was performed in the Static Structural module of ANSYS Workbench.

In the flow field calculation, we simulated turbulence using the standard k - ϵ turbulent model, which is a semi-empirical model of two equations for the turbulent kinetic energy k and the diffusivity ϵ as Eqs. (2) and (3):

$$\frac{\partial}{\partial t}(\rho k) + \frac{\partial}{\partial x_i}(\rho k u_i) = \frac{\partial}{\partial x_j} \left[\left(\mu + \frac{\mu_t}{\sigma_k} \right) \frac{\partial k}{\partial x_j} \right] + G_k + G_b - \rho \epsilon - Y_M + S_k \quad (2)$$

$$\frac{\partial}{\partial t}(\rho \epsilon) + \frac{\partial}{\partial x_i}(\rho \epsilon u_i) = \frac{\partial}{\partial x_j} \left[\left(\mu + \frac{\mu_t}{\sigma_\epsilon} \right) \frac{\partial \epsilon}{\partial x_j} \right] + C_{1\epsilon} \frac{\epsilon}{k} (G_k + C_{3\epsilon} G_b) - C_{2\epsilon} \rho \frac{\epsilon^2}{k} + S_\epsilon \quad (3)$$

where G_k is the turbulent kinetic energy created by the average velocity grads, G_b is the turbulent kinetic energy due to buoyancy, Y_M is the contribution of the fluctuating dilatation in compressible turbulence to the overall dissipation rate, $C_{1\epsilon}$, $C_{2\epsilon}$ and $C_{3\epsilon}$ are constants, σ_k and σ_ϵ are the numbers corresponding to turbulent kinetic energy k and the diffusivity ϵ , S_k and S_ϵ are user-defined source terms.

The fluid field calculation was performed in FLUENT module with the geometric model shown in Fig. 3(a and b), and the specific boundary conditions and parameters were set as follows. The gravitational acceleration was applied in the positive direction of the Z-axis. The fluid rotation speed in the rotor area was set to be the same as the impeller speed. And, the wall of the impeller was set to be a moving wall with the rotation speed the same as the adjacent area. A standard wall surface function was used with the convergence accuracy set to be 0.001. The inlet flow velocity was set to be 0.64 m/s which is the same with the actual flow velocity. The operating

Table 2
Ontogenetic models of strain reinforcement and time reinforcement.

Ontogenetic Model	Principal Equations	Trends
Strain Reinforcement	$\epsilon_{cr} = c_1 \sigma^{c_2} \epsilon^{c_3} e^{-C_4/T}$ ($C_1 > 0, C_3 < 0$)	Strain rate decreases or stabilizes
Time Reinforcement	$\epsilon_{cr} = c_1 \sigma^{c_2} t^{c_3} e^{-C_4/T}$ ($C_1 > 0, -1 < C_3 < 0.5$)	Strain rate decreases or stabilizes

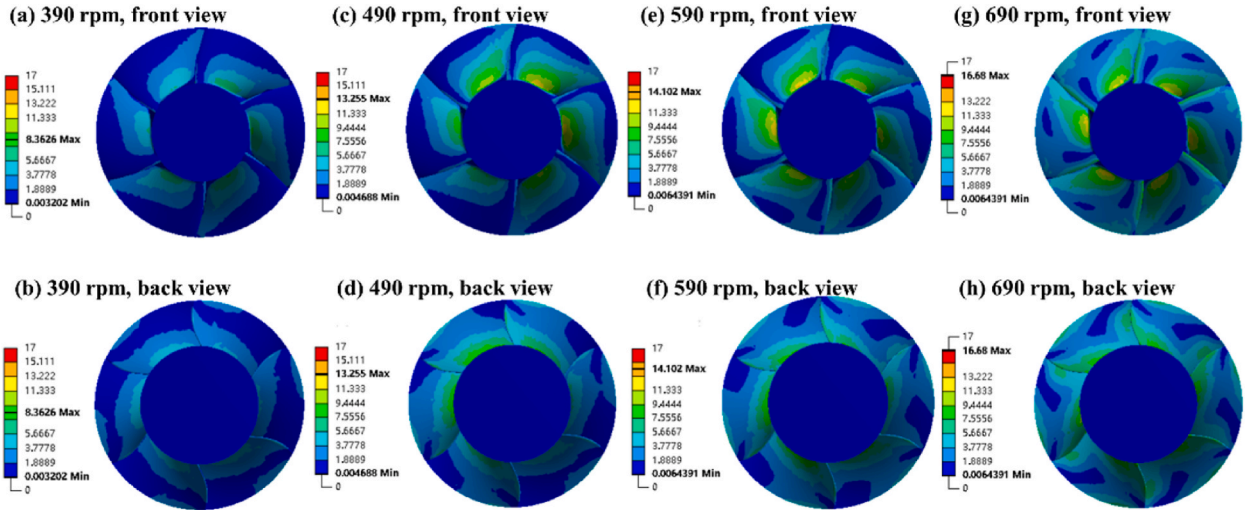


Fig. 4. Equivalent von-Mises stress distribution of the impeller at different rotation speeds of 390 r/min in (a) front view and (b) back view, 490 r/min in (c) front view and (d) back view, 590 r/min in (e) front view and (f) back view, and 690 r/min in (g) front view and (h) back view.

temperature was 350 °C (623 K). The rotor area rotation origin was (0, 0, 0) with Z-axis as the rotation axis, and different rotation speeds of 390, 490, 590, and 690 r/min were adopted to study the effect of rotation speeds on the impeller.

Newton's second law of Eqs. (4) and (5) can be used to construct the conservation equation for the solid domain shown below.

$$\rho_s \ddot{a}_s = \nabla \cdot \sigma_s + f_s \tag{4}$$

$$\frac{\partial(\rho h)}{\partial t} - \frac{\partial \rho}{\partial t} + \nabla \cdot (\rho_j v h) = \nabla \cdot (\lambda \nabla T) + \nabla \cdot (v \tau) + v \cdot \rho f_s + S_E \tag{5}$$

In the structural field calculation, the impeller material was selected as 316L stainless steel. Based on the flow field calculation, the LBE loading could be obtained. And then, the LBE loading was uploaded to the static module and the data transmission was realized through the coupling surface in the static module. According to Hamilton's principle, the structural dynamic equation is defined as Eq. (6):

$$M\ddot{u} + C\dot{u} + Ku = F \tag{6}$$

The stress equation for the impeller structure calculation is as Eqs. (7) and (8):

$$K\{\mu\} = \{F_s\} + \{F_t\} \tag{7}$$

$$\{\sigma\} = DB\{\mu\} \tag{8}$$

The equivalent stress can be obtained based on the von-Mises theory as Eq. (9):

$$\sigma_o = \sqrt{\frac{1}{2}[(\sigma_1 - \sigma_2)^2 + (\sigma_1 - \sigma_3)^2 + (\sigma_3 - \sigma_2)^2]} \tag{9}$$

where σ_o is the equivalent stress (Pa) of each node, σ_1 , σ_2 and σ_3 are the first, second and third principal stresses (Pa), respectively. The pressure results calculated in Fluent were imported into the analysis of the structural field through coupling, and the displacement constraints were applied to the impeller by setting the displacements in the X, Y, and Z directions to 0 mm. The stress distribution of the impeller could be obtained in the structural field calculation.

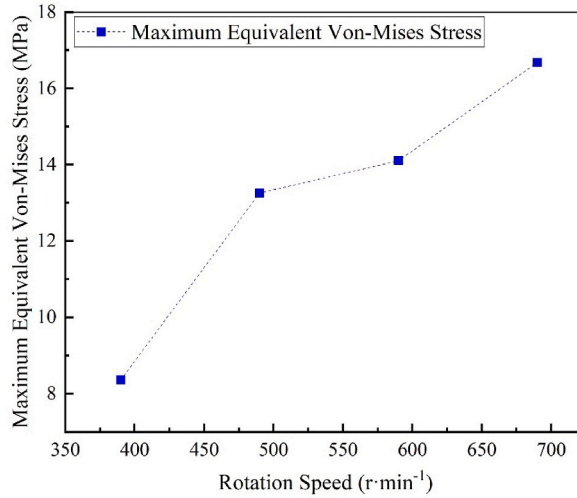


Fig. 5. Relationship between the maximum equivalent von-Mises stress of the impeller and the rotation speed.

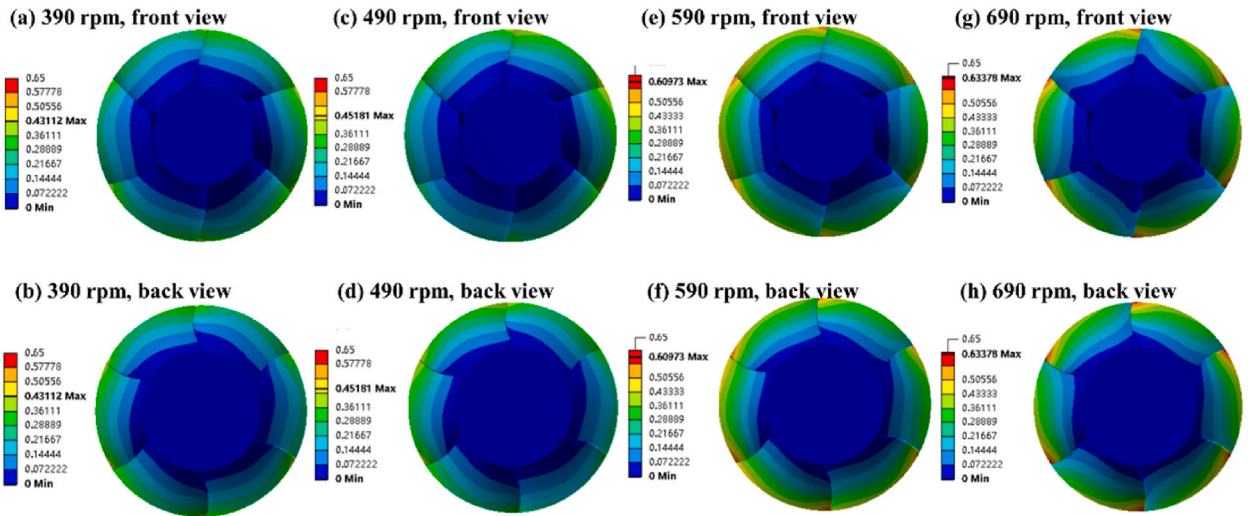


Fig. 6. Deformation distribution of the impeller at different rotation speeds of 390 r/min in (a) front view and (b) back view, 490 r/min in (c) front view and (d) back view, 590 r/min in (e) front view and (f) back view, and 690 r/min in (g) front view and (h) back view.

2.4. Creep calculation

Since the melting point of 316L stainless steel is around 1400 °C and the working temperature in liquid LBE is 350 °C–550 °C, the working temperature of the impeller is 37.2%–49.2% of its melting point in Kelvin temperature. Therefore, the creep effect of the impeller in service needs to be considered. Two basic reinforcement criteria for creep effect were proposed [37,38] as time reinforcement and strain reinforcement as shown in Table 2.

where σ is the equivalent force, ϵ is the equivalent effect variation, t is the time, e is the natural number, T is the absolute temperature, and C_n is the material parameter. When creep calculations were performed, the time-reinforced model was used in this study as Eq. (10) [37]:

$$\epsilon_{cr} = 2 \times 10^{-4} \sigma^{0.224} t^{-0.92865} e^{-246.5/T} \tag{10}$$

As shown in Eq. (10), the creep constants $C1$ – $C4$ are defined as 0.0002, 0.2224, -0.92865 , and 246.5. The boundary conditions were set from the pressure and stress on the impeller obtained in the fluid-solid coupling calculation. The whole calculation time in the creep calculation was set to be 90000 s. According to the above methods, the data transfer between the fluid flow calculation and the structural field calculation can be realized, and the stress, strain and creep characteristics of the impeller in the liquid LBE can be obtained eventually.

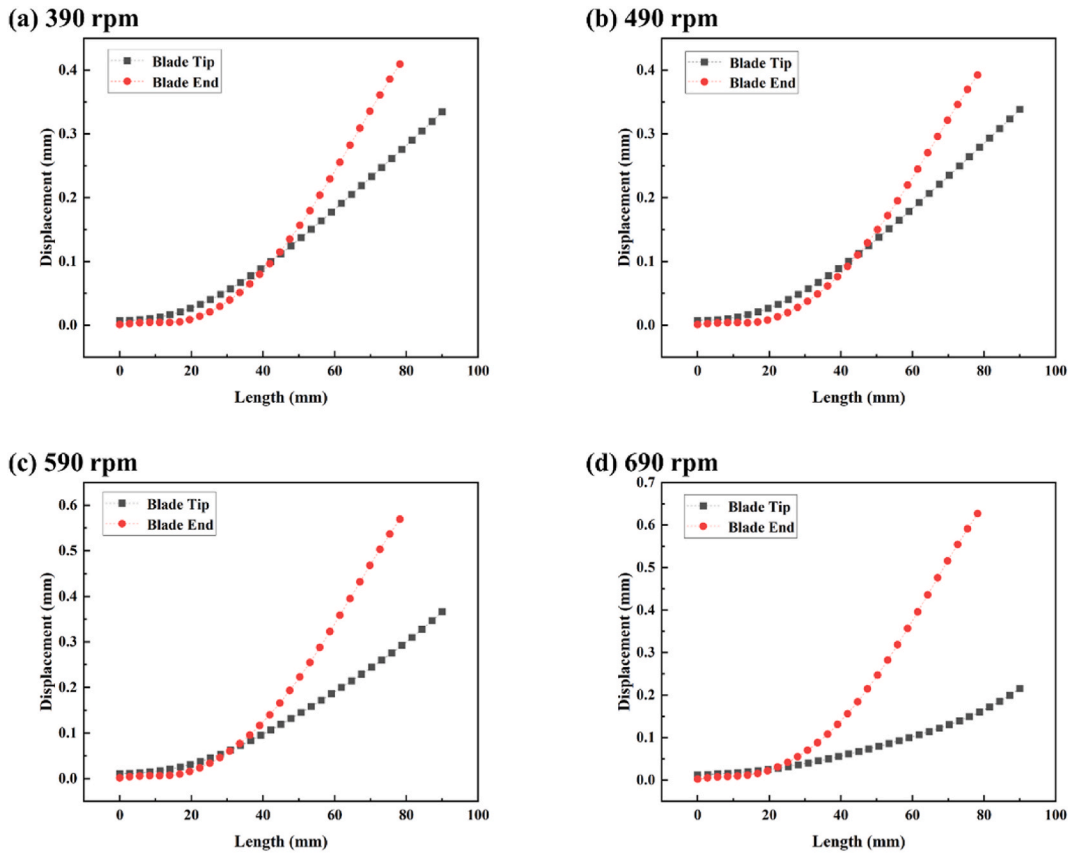


Fig. 7. Deformation distance along both the blade tip and blade tail from the blade root to the blade edge with the rotation speeds of (a) 390 r/min, (b) 490 r/min, (c) 590 r/min, and (d) 690 r/min.

3. Results and discussion

3.1. Stress field and deformation of the impeller

Fig. 4 illustrates the distribution of equivalent von-Mises stress of the impeller under different rotation speeds. It can be seen that, for all rotation speeds in Fig. 4(a–h), the stress concentration regions are mainly located at the root of the blade near the hub, which is consistent with previous publications [13]. However, as the rotation speed increases, the high stress region gradually spreads towards the edge of the blade. In the hub, the equivalent von-Mises stress remains low and does not show a clear trend due to the thick structure. Moreover, the highest equivalent von-Mises stress is found at the root of the blade in all four impellers. At 590 r/min in Fig. 4 (e and f), stress concentration is also observed at the blade edge and inlet side, which intensifies at 690 r/min in Fig. 4(g and h) due to the increased impact of the liquid flow at the inlet side blade. This result indicates that the blade edge and junction between the blade and the hub are susceptible to fatigue damage under continuous loads, while the minimum equivalent von-Mises stress is located at the hub and the blade tip.

To quantitatively analyze the equivalent von-Mises stress of the impeller, the relationship between the maximum equivalent von-Mises stress and the rotation speed is plotted in Fig. 5. The maximum equivalent von-Mises stress of the impeller is found to be only 8.4 MPa when the rotation speed is 390 r/min (Fig. 4(a and b)). However, with the increase of rotation speed, the maximum equivalent von-Mises stress of the impeller tends to increase. At the rotation speed of 690 r/min, the maximum equivalent von-Mises stress reaches 16.7 MPa. It should be noted that the maximum equivalent von-Mises stress of 16.7 MPa is still much less than the yield strength of 316L stainless steel.

In Fig. 6, a deformation distribution of the impeller is displayed at various rotation speeds. It can be observed that the four impellers all exhibit similar deformation patterns, with higher degrees of deformation occurring towards the edge of the blade in Fig. 6(a–h). Additionally, the blades experience more deformation than the hub. At the tip of the blade, the maximum deformation is observed, while the minimum deformation is found at the root of the blade and the hub. The observed deformation behavior can be attributed to pressure loads and centrifugal forces that act on the outer ring of the impeller at the blade edge. Moreover, as the rotation speed increases, both the blade deformation area and magnitude increase.

To quantitatively analyze the deformation of the impeller, the values of the deformation distance along both the blade tip and blade

Table 3

Quantitative information of equivalent von-Mises stress and deformation of impeller under different rotation speeds.

Rotation Speed (r/min)	Maximum Equivalent von-Mises Stress (MPa)	Maximum Deformation (mm)	Maximum Deformation Position
390	8.4	0.43	Blade tip
490	13.3	0.45	Blade tip
590	14.1	0.61	Blade tip and blade tail
690	16.7	0.63	Blade tail

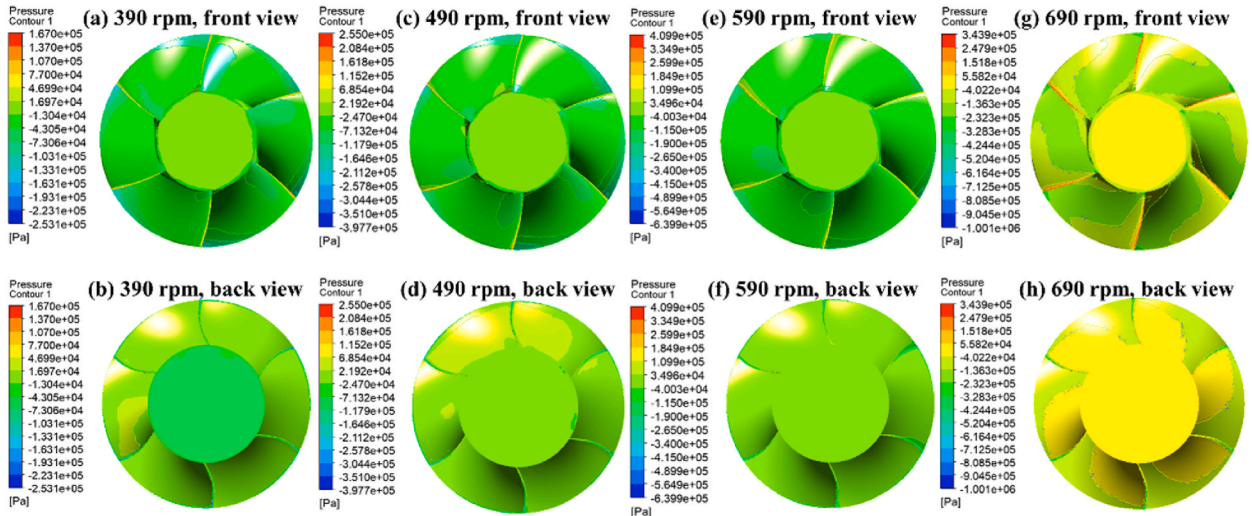


Fig. 8. Imported pressure distribution of impeller at different rotation speeds of 390 r/min in (a) front view and (b) back view, 490 r/min in (c) front view and (d) back view, 590 r/min in (e) front view and (f) back view, and 690 r/min in (g) front view and (h) back view.

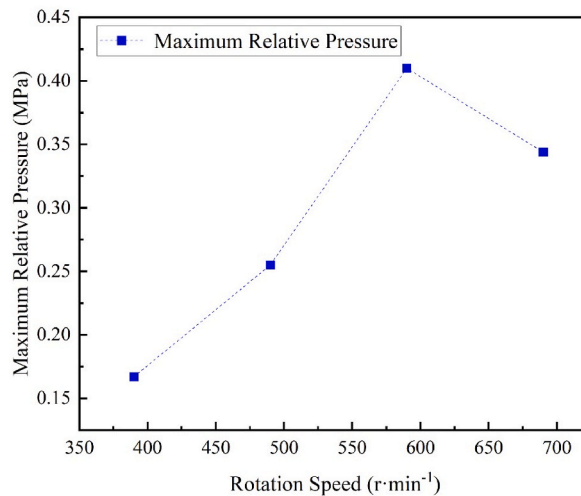


Fig. 9. Relationship between the maximum imported pressure and the rotation speed.

tail from the blade root to the blade edge were recorded as shown in Fig. 7. It can be seen that with the increase of the distance to the blade root, the value of the deformation displacement increases. When the rotation speed is 390 r/min, the maximum deformation is 0.43 mm which occurs at the end of the blade tail in Fig. 7(a). With the increase of the rotation speed, the value of the maximum deformation has a trend to increase as in Fig. 7(a–d). At the rotation speed of 690 r/min, the maximum deformation is 0.63 mm, as shown in Fig. 7(d). It is also found that the deformation occurred at the blade tail is relatively larger than that at the blade tip. The higher the rotation speed, the larger the difference between the deformation occurred at the blade tail and the blade tip.

Quantitative information on the equivalent von-Mises stress and deformation of the impeller at various rotation speeds is recorded as shown in Table 3. It can be observed that, under established working conditions, the maximum equivalent von-Mises stress within

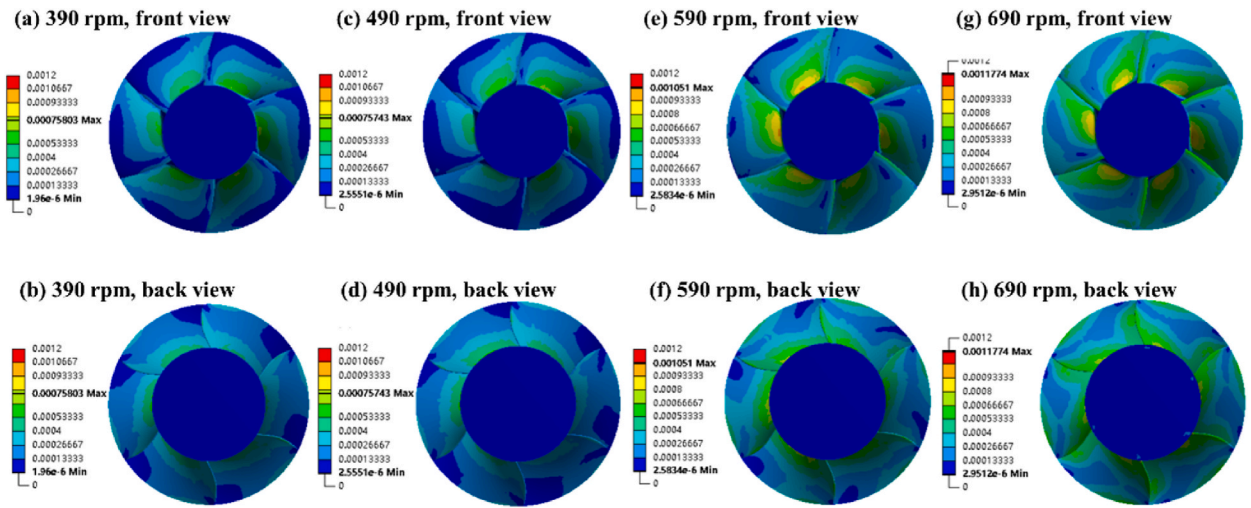


Fig. 10. The creep deformation distribution of impeller at different rotation speeds of 390 r/min in (a) front view and (b) back view, 490 r/min in (c) front view and (d) back view, 590 r/min in (e) front view and (f) back view, and 690 r/min in (g) front view and (h) back view.

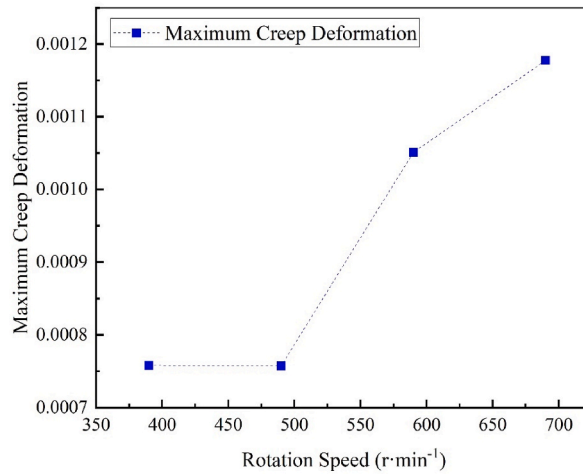


Fig. 11. Relationship between the maximum equivalent creep strain and the rotation speed.

the give rotation speed range does not exceed 20 MPa, which is much less than the yield strength of 316L stainless steel. Additionally, the maximum deformation is less than 0.65 mm. Therefore, the results of the fluid-solid coupling analysis indicate that the impeller is able to function properly in a liquid LBE environment.

3.2. Creep deformation of the impeller

The fluid-solid coupling calculation yields the pressure loading on the impeller’s surface, which serves as the initial condition for the subsequent creep calculation. Fig. 8 shows the imported pressure distribution of the impeller at different rotation speeds. Positive values indicate compressive pressure, while negative values denote tensile pressure. In the front view in Fig. 8(a–c, e, g), the pressure distribution is uniform across the blade and the hub, with the hub experiencing relatively higher fluid pressure than the blade surface. However, the maximum pressure is primarily concentrated at the blade tip, which is the thinnest and experiences the strongest fluid impact. With increasing rotation speed, the imported pressure value of the impeller also increases, with the minimum being located at the blade edge and the maximum at the blade tip in Fig. 8(a–h).

Fig. 9 shows the relationship between the maximum imported pressure and the rotation speed. It can be seen that the maximum imported pressure has an increasing trend as the rotation speed increases. However, the maximum imported pressure decreases when the rotation speed is 690 r/min. The maximum value of 0.410 MPa occurs at the rotation speed of 590 r/min, and the minimum value of 0.167 MPa occurs at the rotation speed of 390 r/min.

Fig. 10 displays the equivalent creep strain distribution of the impeller under different rotation speeds. The equivalent creep strain

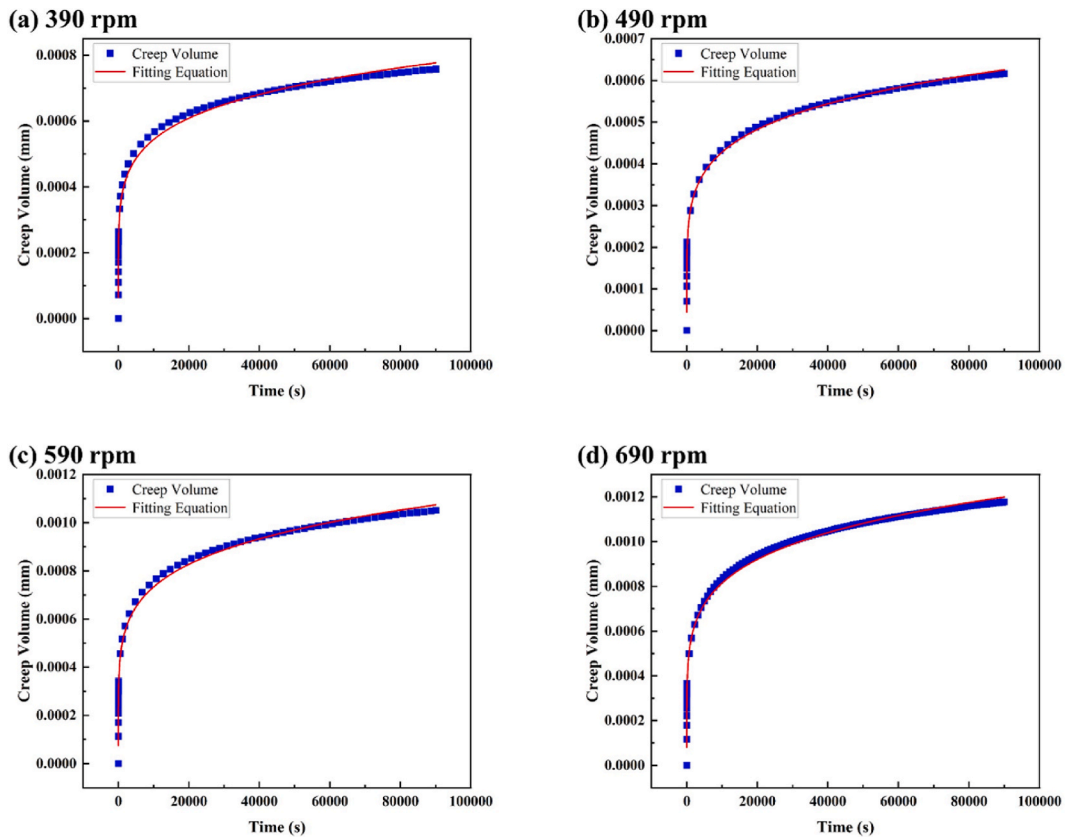


Fig. 12. Creep volume of the impeller as a function of time at different rotation speeds of: (a) 390 r/min, (b) 490 r/min, (c) 590 r/min, and (d) 690 r/min.

at the blade edge and hub is insignificant, while that at the root and middle of the blade is significant. The highest strain occurs at the blade root near the hub as shown in Fig. 10(a–h). An upward trend in the maximum equivalent creep strain of the impeller is observed with an increase in rotation speed, occurring progressively from the blade root to the middle and the entirety of the blade. The minimum equivalent creep strain of the impeller, measured at a rotation speed of 490 r/min in Fig. 10(c and d), is 0.076%, while the maximum creep deformation, measured at a rotation speed of 690 r/min in Fig. 10(g and h), is 0.118%. Overall, the impeller's creep deformation tends to increase, as shown in Fig. 11.

3.3. Creep curve fitting equation

It should be noted that the creep deformation as mentioned above was obtained at 90000 s, which is 25 h. However, the impeller should work in a stable condition for several years in reality. In this study, the creep results for years were obtained by the extension of the above calculated results. Fig. 12 shows the creep strain of the impeller as a function of time and the fitting curves at different rotation speeds. The fitting equations can be obtained as Eq. (11):

$$y = at^b \quad (11)$$

For the rotation speeds of 390, 490, 590, and 690 rpm in Fig. 12(a–d), the parameters of a are 1.2143×10^{-4} , 0.8694×10^{-4} , 1.4772×10^{-4} , and 1.6048×10^{-4} , and the parameters of b are 0.1627, 0.1730, 0.1739, and 0.1763. It can be seen that the creep amount tends to increase with the increasing time. At the initial stage, the creep deformation volume increases fast, and increasing rate of the creep deformation volume gradually decreases with time. At the rotation speed of 490 r/min in Fig. 12(b), the creep of the impeller working for five years is 0.228%. At the rotation speed of 690 r/min in Fig. 12(d), the creep of the impeller working for five years reaches its maximum which is 0.447%. Therefore, the austenitic stainless-steel impeller can work normally in the liquid LBE environment for at least 5 years under the working conditions considering creep.

4. Conclusions

The study aimed to investigate the stress, deformation, and creep characteristics of the nuclear main pump impeller in a liquid lead-bismuth environment at various rotational speeds. The main conclusions are as follows:

- (1) At the flow rate of 0.64 m/s and speed of 690 r/min, the maximum equivalent force is 16.7 MPa, which is much smaller than the yield strength of 316L stainless steel, while the maximum deformation is less than 0.63 mm, indicating that the impeller can ensure normal operation in the liquid lead bismuth environment.
- (2) The maximum stress, deformation, and creep of the impeller blade generally exhibit an increasing trend with the increase in rotation speed. The junction of the blade root and hub is particularly prone to stress concentration and fatigue damage. Therefore, it is important to pay close attention to this area during impeller design.
- (3) At a flow rate of 0.64 m/s, the creep of the impeller over a five-year period ranges from a minimum of 0.228% to a maximum of 0.447%. These results indicate that the austenitic stainless steel impeller is capable of functioning properly in a liquid lead bismuth environment for at least five years.

Data availability

All data that support the findings of this study are available from the corresponding author upon reasonable request.

Additional information

No additional information is available for this paper.

CRediT authorship contribution statement

Cheng Gu: Writing – review & editing, Methodology, Investigation, Conceptualization. **Weili Peng:** Writing – original draft, Visualization, Software. **Zenghui Tian:** Writing – review & editing, Visualization. **Jianhua Zhao:** Investigation, Funding acquisition, Conceptualization. **Fan Wang:** Writing – review & editing, Validation. **Yajun Wang:** Writing – review & editing, Validation, Investigation. **Jiaxuan Zhang:** Software, Formal analysis.

Declaration of competing interest

The authors declare that they have no known competing financial interests or personal relationships that could have appeared to influence the work reported in this paper.

Acknowledgments

The authors would like to acknowledge the financial supports from the National Natural Science Foundation of China (No. 51875062, No. 52205336) and the China Postdoctoral Science Foundation (No. 2021M700567).

References

- [1] A. Alemberti, M. Caramello, M. Frignani, G. Grasso, F. Merli, G. Morresi, M. Tarantino, ALFRED reactor coolant system design, *Nucl. Eng. Des.* 370 (2020) 110884, <https://doi.org/10.1016/j.nucengdes.2020.110884>.
- [2] R. Yu, L. Gu, X. Sheng, J. Li, Y. Zhu, L. Zhang, W. Jiang, Review of fuel assembly design in lead-based fast reactors and research progress in fuel assembly of China initiative accelerator driven system, *Int. J. Energy Res.* 45 (2021) 11552–11563, <https://doi.org/10.1002/er.6569>.
- [3] Y. Zhang, C. Wang, Z. Lan, S. Wei, R. Chen, W. Tian, G. Su, Review of thermal-hydraulic issues and studies of lead-based fast reactors, *Renew. Sustain. Energy Rev.* 120 (2020) 109625, <https://doi.org/10.1016/j.rser.2019.109625>.
- [4] L. Martinelli, K. Ginestar, V. Botton, C. Delisle, F. Balbaud-Célérier, Corrosion of T91 and pure iron in flowing and static Pb-Bi alloy between 450 °C and 540 °C: experiments, modelling and mechanism, *Corrosion Sci.* 176 (2020), <https://doi.org/10.1016/j.corsci.2020.108897>.
- [5] X. Gong, M.P. Short, T. Auger, E. Charalampopoulou, K. Lambrinou, Environmental degradation of structural materials in liquid lead- and lead-bismuth eutectic-cooled reactors, *Prog. Mater. Sci.* 126 (2022) 100920, <https://doi.org/10.1016/j.pmatsci.2022.100920>.
- [6] J. Zhang, Lead-bismuth eutectic (LBE): a coolant candidate for Gen. IV advanced nuclear reactor concepts, *Adv. Eng. Mater.* 16 (2014) 349–356, <https://doi.org/10.1002/adem.201300296>.
- [7] X. Li, X. Zeng, Z. Zhao, X. Zhang, Q. Yan, Y. Zhang, Y. Wen, X. Yang, F. Mao, Fast-flowing LBE corrosion of the SiC pump impeller: numerical and experimental investigations, *Int. J. Appl. Ceram. Technol.* 20 (2023) 436–450, <https://doi.org/10.1111/ijac.14201>.
- [8] Y. Wang, B. Jing, C. Gao, A contrast between classical method and finite element method for calculating strength in impeller of centrifugal pump, *J. Vibroengineering*. 17 (2015) 3261–3270.
- [9] Z. Zhai, C. Li, H. Cui, H. Liang, H. Cheng, Fatigue life prediction for throwing impeller of an impeller blower, *Int. J. Perform. Eng.* 15 (2019) 127–137, <https://doi.org/10.23940/ijpe.19.01.p13.127137>.
- [10] X. Chen, D. Yuan, M. Yang, S. Yuan, Blade stress of the reactor coolant pump of 300 MWe nuclear power plant in China based on fluid-solid coupling method, *Jixie Gongcheng Xuebao/Journal Mech. Eng.* 46 (2010) 111–115, <https://doi.org/10.3901/JME.2010.04.111>.
- [11] X. Wang, Y. Lu, R. Zhu, Q. Fu, H. Yu, Y. Chen, Study on bidirectional fluid-solid coupling characteristics of reactor coolant pump under steady-state condition, *Nucl. Eng. Technol.* 51 (2019) 1842–1852, <https://doi.org/10.1016/j.net.2019.05.009>.
- [12] X.D. Ma, X.L. Li, Z.Q. Zhu, C.J. Li, S. Gao, The stress analysis of a heavy liquid metal pump impeller, *IOP Conf. Ser. Mater. Sci. Eng.* 129 (2016), <https://doi.org/10.1088/1757-899X/129/1/012023>.
- [13] X. Liu, F. Xu, L. Cheng, W. Pan, W. Jiao, Stress characteristics analysis of vertical Bi-directional flow channel axial pump blades based on fluid-structure coupling, *Machines* 10 (2022), <https://doi.org/10.3390/machines10050368>.
- [14] F. Yang, D. Jiang, W. Hu, A. Nasr, C. Liu, R. Xie, Dynamic stress characteristics and fatigue life analysis of a slanted axial-flow pump, *Proc. Inst. Mech. Eng. Part C J. Mech. Eng. Sci.* (2022), <https://doi.org/10.1177/09544062221141555>.
- [15] J. Pei, F. Meng, Y. Li, S. Yuan, J. Chen, Fluid-structure coupling analysis of deformation and stress in impeller of an axial-flow pump with two-way passage, *Adv. Mech. Eng.* 8 (2016) 1–11, <https://doi.org/10.1177/1687814016646266>.

- [16] D. Zhang, D. Pan, Y. Xu, P. Shao, G. Wang, Numerical investigation of blade dynamic characteristics in an axial flow pump, *Therm. Sci.* 17 (2013) 1511–1514, <https://doi.org/10.2298/TSCI1305511Z>.
- [17] B. Li, H. Zhang, L. Zang, Static Stress and modal analysis of the impeller of the high-pressure low-flow pump, *Appl. Mech. Mater.* 117–119 (2012) 430–433, <https://doi.org/10.4028/www.scientific.net/AMM.117-119.430>.
- [18] J. Lin, Y. Jin, Z. Zhang, X. Cui, Strength analysis of the carbon-fiber reinforced polymer impeller based on fluid solid coupling method, *Math. Probl Eng.* 2014 (2014), <https://doi.org/10.1155/2014/803261>.
- [19] W. Li, L. Ji, W. Shi, L. Zhou, X. Jiang, Y. Zhang, Vibration characteristics of the impeller at multi-conditions in mixed-flow pump under the action of fluid-structure interaction, *J. Vibroengineering.* 18 (2016) 3213–3224, <https://doi.org/10.21595/jve.2016.16776>.
- [20] J. Yang, G. Fang, D. Hu, Z. Cai, J. Zhai, Y. Zheng, K. Kan, Hydrodynamic and structural stability analysis for shaft tubular pump unit, *IOP Conf. Ser. Earth Environ. Sci.* 647 (2021), <https://doi.org/10.1088/1755-1315/647/1/012038>.
- [21] X.L. Tang, Y.X. Jia, F.J. Wang, D.Q. Zhou, R.F. Xiao, W. Yang, Y.L. Wu, Investigations of turbulent flows in a tubular pump and structural stresses of its impeller, *IOP Conf. Ser. Earth Environ. Sci.* 15 (2012) 1–9, <https://doi.org/10.1088/1755-1315/15/5/052012>.
- [22] Y. Li, H. Su, Y. Wang, W. Jiang, Q. Zhu, Dynamic characteristic analysis of centrifugal pump impeller based on fluid-solid coupling, *J. Mar. Sci. Eng.* 10 (2022), <https://doi.org/10.3390/jmse10070880>.
- [23] S. Yong, W. Donglei, J. Tao, L. Yanwei, Modal analysis on impeller rotor of the axial flow pump based on fluid-structure interaction, *IOP Conf. Ser. Earth Environ. Sci.* 376 (2019), <https://doi.org/10.1088/1755-1315/376/1/012023>.
- [24] X. Cheng, X. Liu, B. Lv, Influence of the impeller/guide vane clearance ratio on the performances of a nuclear reactor coolant pump, *Fluid Dynam. Mater. Process.* 18 (2022) 93–107, <https://doi.org/10.32604/fdmp.2022.017566>.
- [25] X. Zheng, L. Jin, T. Du, B. Gan, F. Liu, H. Qian, Effect of temperature on the strength of a centrifugal compressor impeller for a turbocharger, *Proc. Inst. Mech. Eng. Part C J. Mech. Eng. Sci.* 227 (2013) 896–904, <https://doi.org/10.1177/0954406212454966>.
- [26] F. Meng, S. Yuan, Y. Li, Fluid–structure coupling analysis of impeller in unstable region for a reversible axial-flow pump device, *Adv. Mech. Eng.* 10 (2018) 1–10, <https://doi.org/10.1177/1687814017751762>.
- [27] X. Chen, Y. Zheng, J. Xu, Y. Zhang, E. Fernandez-Rodriguez, C. Li, Y. Zhou, T. Jiang, Fatigue life study of francis pump under reverse generation condition based on fluid solid coupling, *Water (Switzerland)* (2020) 12, <https://doi.org/10.3390/W12041162>.
- [28] Y. Zhou, W. Hu, Y. Zhou, Y. Zheng, Analysis of pressure fluctuation and stress deformation in reverse generation of large vertical axial flow pump, *IOP Conf. Ser. Earth Environ. Sci.* 237 (2019), <https://doi.org/10.1088/1755-1315/237/3/032093>.
- [29] H. Li, M. Gu, M. Tang, Modal simulation of turbocharger impeller with considering fluid-solid interaction, *J. Vibroengineering.* 18 (2016) 485–495.
- [30] C. Wang, W. Shi, Q. Si, L. Zhou, Numerical calculation and finite element calculation on impeller of stainless steel multistage centrifugal pump, *J. Vibroengineering.* 16 (2014) 1723–1734.
- [31] J. Yuan, J. Shi, Y. Fu, H. Chen, R. Lu, X. Hou, Analysis of fluid-structure coupling dynamic characteristics of centrifugal pump rotor system, *Energies* 15 (2022), <https://doi.org/10.3390/en15062133>.
- [32] A.R. Al-Obaidi, Investigation of the influence of various numbers of impeller blades on internal flow field analysis and the pressure pulsation of an axial pump based on transient flow behavior, *Heat Transf* 49 (2020) 2000–2024, <https://doi.org/10.1002/hjt.21704>.
- [33] D. Zindani, A.K. Roy, K. Kumar, Design of mixed ow pump impeller blade using mean streamline theory and its analysis, *Sci. Iran.* 27 (2020) 350–360, <https://doi.org/10.24200/sci.2018.20829>.
- [34] A. Hussein, L. Hao, C. Yan, R. Everson, Finite element simulation of the temperature and stress fields in single layers built without-support in selective laser melting, *Mater. Des.* 52 (2013) 638–647, <https://doi.org/10.1016/j.matdes.2013.05.070>.
- [35] Z. Su, T. Zhou, M. Liu, W. Zou, *Thermophysical Properties of Liquid Lead-Bismuth Eutectic*, vol. 36, He Jishu/Nuclear Tech, 2013.
- [36] K. Jalammanavar, N. Pujar, R. Vishnu Raj, Finite element study on mesh discretization error estimation for ansys Workbench, *Proc. Int. Conf. Comput. Tech. Electron. Mech. Syst. CTEMS 2018* (2018) 344–350, <https://doi.org/10.1109/CTEMS.2018.8769258>.
- [37] J. Chen, Q. Jiang, Y. Hu, W. Qin, S. Li, J. Xiong, Time-dependent performance of damaged marble and corresponding fractional order creep constitutive model, *Arabian J. Geosci.* 13 (2020), <https://doi.org/10.1007/s12517-020-06109-9>.
- [38] S. Nadimi, K. Shahriar, Experimental creep tests and prediction of long-term creep behavior of grouting material, *Arabian J. Geosci.* 7 (2014) 3251–3257, <https://doi.org/10.1007/s12517-013-0920-7>.